

Article

Hybrid Superconducting/Superconducting Mesoscopic Heterostructure Studied by Modified Ginzburg–Landau Equations

Jesús González * , Angélica Melendez and Luis Camargo 

Faculty of Engineering del Magdalena, Universidad del Magdalena, Carrera 32 No 22-08, Santa Marta 470004, Magdalena, Colombia; melangie2015@gmail.com (A.M.); lcamargoa@unimagdalena.edu.co (L.C.)

* Correspondence: jgonzaleza@unimagdalena.edu.co

Abstract: Studies involving vortices in hybrid superconducting devices and their interactions with different components inside samples are important for reaching higher values of critical parameters in superconducting materials. The vortex distribution on each side of a sample with different fundamental parameters, such as temperature T , penetration depth λ , coherence length ξ , electron mass m , and the order parameter Ψ , may help to improve the superconducting properties. Thus, in this work, we used the modified Ginzburg–Landau theory to investigate a hybrid superconductor (HS), as well as to provide a highly tunable and adjustable theoretical tool for theoretically explaining the experimental results involving the HS in order to study the vortex behavior in superconductors of mesoscopic dimensions with extreme differences among their fundamental parameters. Therefore, we evaluated the influence of the HS on the vortex configuration and its effects on field-dependent magnetization. The results show that when the applied magnetic field H was increased, the diamagnetic response of the HS (Meissner effect) included additional jumps in magnetization, while diamagnetism continued to increase in the sample. In addition, the differences among parameters created an interface between both components, and two different magnitudes of supercurrent and vortex sizes caused less degradation of the local superconductivity, which increased the upper critical field. On the other hand, this type of HS with differences in parameters on both sides can be used to control the vortex movement in the selected sample of the superconducting region with more accuracy.



Citation: González, J.; Melendez, A.; Camargo, L. Hybrid Superconducting/Superconducting Mesoscopic Heterostructure Studied by Modified Ginzburg–Landau Equations. *Condens. Matter* **2023**, *8*, 104. <https://doi.org/10.3390/condmat8040104>

Academic Editors: Andrea Perali, Milorad Milosevic, Roberta Citro and David Neilson

Received: 19 September 2023

Revised: 7 November 2023

Accepted: 20 November 2023

Published: 1 December 2023



Copyright: © 2023 by the authors. Licensee MDPI, Basel, Switzerland. This article is an open access article distributed under the terms and conditions of the Creative Commons Attribution (CC BY) license (<https://creativecommons.org/licenses/by/4.0/>).

Keywords: vortex; superconductivity; Ginzburg–Landau theory; magnetization; free energy

1. Introduction

Usually, the interconnection of materials at the quantum level with superconducting condensates leads to a leakage of Cooper pairs through heterointerfaces, which is known as the proximity effect [1]. This procedure has become a route to the design of superconducting electronics and the engineering of new quantum states. This includes the development of hybrid quantum devices, which have opened an important area in research based on advances in fabricating nanostructures with highly controllable accuracy, thus allowing their physical and electronic properties, as well as their power consumption, to be manipulated and tailored. Research on hybrid superconducting structures, which are made up of a superconductor and non-superconducting material, takes the proximity effect into account, as this explains the correlations of adjacent non-superconducting layers [2–8]. The freedom in the design and fabrication of the heterostructures of emergent two-dimensional (2D) materials [9,10] has opened the possibility for research on the interactions of fundamental properties at the nanoscale. Such research results show that it is possible to control the critical temperature, critical magnetic field, and energy gaps in selected regions as a result of the creation of tailored nanostructured superconductors with complex superconductor materials for applications in quantum technology. These developments have allowed new advances, including the superconducting proximity effect in epitaxial graphene induced by a graphene–superconductor interface [11]. Numerical calculations have shown many effects

that are usually observed in nanostructured superconductors, and these result in complex vortex patterns when barriers or defects are included [12–17]. Additionally, the inclusion of anisotropies in superconducting samples through variations in T_c in different layers of the sample leads to distinct vortex states and free-energy curves [18–20], as well as new possibilities for non-conventional vortex structures [21]. These kinds of systems exhibit a variety of new and interesting phenomena with no counterparts in conventional single-component superconductors [22]. Exotic vortex structures can emerge in a two-component superconductor because of the different length scales ζ_i at which the Cooper-pair density varies in each component [23,24]. Two-dimensional superconductivity has been investigated to find insights into a variety of quantum phenomena; the thermal evaporation and sputtering of metallic films allow the study of most of the basic properties of 2D superconductors [25,26]. The methods for fabrication, such as quantum phase transitions, open new discussions and opportunities for the study of thin-film superconductors with thicknesses from 0.3 nm to 10 nm [27,28].

Previously, fabrication techniques, such as molecular beam epitaxy accompanied by surface or interface reconstruction processes and methods for the production of field-effect devices and mechanical exfoliation, were introduced into the field of 2D superconductors [29–31]; as a result, crystallinity has been greatly improved, even in atomically thick samples. The different phenomena associated with hybrid combinations with other superconductors have shown relevant effects, such as the magnetic field-driven quantum phase transition that takes place electrostatically in superconducting interfaces, among other effects [32,33]. In addition, combinations with low-dimensional semiconductors offer a versatile ground for novel device concepts, such as supercurrent transistors, sources of spin-entangled electrons, quantum computation, and nano-SQUIDS. When a superconductor is coupled with another superconductor, very interesting phenomena take place; both condensates interact with each other at the interface, and the supercurrent can be modulated in this region. In this context, the modulated domain–wall superconductivity offers the possibility of controlling the strength of superconductivity at will. The underlying physics behind such hybrid devices ultimately rely on the superconductors that are selected for coupling.

In the present contribution, we study the fundamental properties and vortex matter of hybrid superconducting samples made of two superconductors, in which each component is well known. The desired parameters of the components, as well as the geometry, type, and distribution of each superconductor, are chosen. In our work, we modified the GL formalism in order to study hybrid superconducting samples; the interaction between the two densities of the superconductors and the order parameters that occurred in the interface between the soft and wall domains were modulated with high precision by using the fundamental parameters of each superconductor.

In Section 2, we show the derived GL equations and the ratios of intrinsic parameters of superconductivity, and this procedure is used in the calculations. In Section 3, we analyze the results obtained for hybrid samples with two superconducting components divided into two halves (Figure 1). Further, we discuss the issues concerning the distribution and configuration of vortices in the sample, as well as the phase of the order parameter, the density of the supercurrent, and magnetization. The results are finally summarized in Section 4.

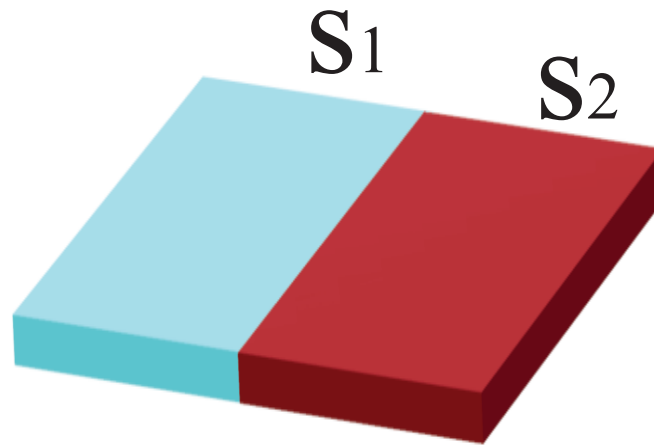


Figure 1. (Color online) Schematic representation of a hybrid superconducting system made of two types of superconductors: S_1 and S_2 . The lateral size of the superconducting sample is $a = 400$ nm, and the width of the sample is $d = 20$ nm. Two cases are studied: 1. S_1 and S_2 are both type II superconductors with the following parameters: a coherence length of $\xi_1(0) = 39$ nm and $\xi_2(0) = 20$ nm and a penetration depth of $\lambda_1(0) = 52$ nm and $\lambda_2(0) = 200$ nm; 2. S_1 is a type II superconductor with the parameters $\xi_1(0) = 39$ nm and $\lambda_1(0) = 52$ nm, but S_2 is a type I superconductor with the parameters $\xi_2(0) = 120$ nm and $\lambda_1(0) = 72$ nm.

2. Materials and Methods

We consider an HS with a thickness d that is smaller than the two characteristic lengths for a superconductor system in such a way that the system is effectively two-dimensional. In this study, the two superconductors inside the sample are denoted as S_1 and S_2 ; the quantities are scaled to units that depend on the parameters of S_1 . The theoretical GL equations were obtained by minimizing the following energy functional:

$$F = \sum_{i=1,2} \int dV [\alpha_i(0) \left(1 - \frac{T}{T_{ci}}\right) |\Psi|^2 + \frac{\beta_i}{2} |\Psi|^4 + \frac{1}{2m_i^*} \times \left| \left(-i\nabla - \frac{2e}{c} \mathbf{A}\right) \Psi \right|^2 + \frac{(\mathbf{H} - \mathbf{H}_a)^2}{8\pi}], \quad (1)$$

where \mathbf{H}_a denotes the applied magnetic field, \mathbf{H} is the total local magnetic field, which includes the response of the superconductor, and the index i represents either S_1 or S_2 depending on the location inside the volume V . We include an additional component that scales the functional to the parameters of S_1 with the variables α_1 , β_1 , and m_1^* . Now, by minimizing Equation (1), we obtain the following for the order parameter and vector potential:

$$-(1 - c_T t) \frac{1}{c_\xi} \psi + \frac{c_\lambda c_m^2}{c_\xi} |\psi|^2 \psi + (-i\nabla - \mathbf{A})^2 \psi = 0 \quad (2)$$

$$j_s = \kappa_1^2 (\nabla \times \nabla \times (\mathbf{A} - \mathbf{A}_0)) = c_m \Re(\psi^* (-i\nabla - \mathbf{A}) \psi), \quad (3)$$

with the following boundary condition:

$$\mathbf{n} \cdot (-i\nabla - \mathbf{A}) \psi|_{S_s} = 0, \quad (4)$$

where the parameters are defined as $c_T = T_{c,1}/T_{c,2}$, $c_\xi = \xi_2^2(0)/\xi_1^2(0)$, $c_\lambda = \lambda_2^2(0)/\lambda_1^2(0)$, $c_m = m_1^*/m_2^*$, and $t = T/T_{c,1}$; in addition, c_m , c_λ , c_ξ , and c_T are used. The above equations are given in dimensionless form; distances are measured in units of $\xi_1(0) = \sqrt{-\hbar^2/2m\alpha_1(0)}$, the temperature is measured in units of the critical temperature of S_1 ($T_{c,1}$), the order parameter Ψ is measured in units of $\Psi_{\infty,1} = \sqrt{-\alpha_1(0)/\beta_1}$, the vector potential is measured in units of $A_{0,1} = c\hbar/2e\xi_1^2(0)$, the magnetic field is measured in units

of the upper critical field of S_1 , $H_{c2,1} = c\hbar/2e\xi_1^2(0)$, and the free energy is measured in units of $F_0 = \alpha_1^2(0)/\beta_1$. The region in the sample where an additional superconductor is included to obtain a two-component superconducting thin film can be directly modeled by changing the parameters c_T , c_{ξ} , c_{λ} , and c_m . In other words, many types of two-component superconducting systems can be studied by tuning the parameters with the desired precision. We solve the coupled GL equations self-consistently by using the link variable approach for a finite-difference representation of the order parameter and the vector on a uniform two-dimensional Cartesian grid (x, y) . The order parameter is calculated by using the first GL equation. The second GL equation is then used to find the supercurrent, and by using the Fourier transform of the supercurrent, the vector potential is calculated; this, again, is used as an input for the first GL equation until a convergent solution for both ψ and \mathbf{A} is found. The extended derivation of GL equations can be detailed in Appendix A.

3. Results and Discussion

The two superconductors inside of the sample (S_1 and S_2) each denote half of the nanostructure; the quantities are scaled to units that depend on the parameters of S_1 . The lateral size of the considered square superconducting sample is $a = 400$ nm, and the width is $d = 20$ nm. This simulation includes two kinds of type II superconductors for the two halves; we chose the following parameters in superconductor 1 (S_1) and superconductor 2 (S_2): a coherence length of $\xi_1(0) = 39$ nm and $\xi_2(0) = 20$ nm; a penetration depth of $\lambda_1(0) = 52$ nm and $\lambda_2(0) = 200$ nm; a critical temperature of $T_{c1} = 9.25$ K and $T_{c2} = 8.0$ K. In addition, the temperature used in the system was $T = 6$ K, and the parameters were $c_{\xi} = 0.26$, $c_{\lambda} = 14.79$, $c_T = 1.15$, $\tau = 0.65$, and $c_m = 1$.

As an example, we chose the coherence length and penetration depth so that the difference between both Ginzburg–Landau (GL) parameters in the sample was large in order to establish a substantial difference between the components and appreciate the behavior of their physical quantities. To begin with, the variation in the magnetization was analyzed in the hybrid heterostructure due to the entrance of vortices into both superconducting components, as illustrated in Figure 2 (left). When the vortices entered into the sample made with one superconducting component, this routinely led to a decrease in the magnetization showing jumps. However, the results in the HS showed that after one jump, in which the magnetization should have decreased, the Meissner effect still grew with the increase in the applied magnetic field, and a new jump in magnetization took place. (See the snapshot of the magnetization curve in Figure 2 (top) point (a) and (b).)

Figure 2 (right) shows contour plots of the density of the superconducting order parameter for different selected vortex states (first column) and the corresponding phase of the order parameter (second column). The total angular momentum L through $\Psi = \psi \exp(iL\phi)$ was used to characterize the vortex state. The effective angular momentum was $L = \Delta\phi/2\pi$; for each clockwise path going from red to blue, a vortex was found: $L = 1, 2, 3, \dots$. Because L_1 represents the number of vortices in S_1 , we use L_2 for S_2 . After nucleation at the sample surface, the superconducting order parameter $|\Psi|$ was trapped inside the hybrid sample, which had a flux of $L\phi_0$, where ϕ_0 is the quantum flux.

As seen in snapshot (a) of the first column of Figure 2 (right), which corresponds to the states $L_1 = 0$ and $L_2 = 2$, the first vortex lines to enter penetrated the sample in S_2 . The increment in the jump in magnetization was modified by the entrance of magnetic flux into the sample, which was proportional to the size of the vortex. There was a large contribution to $-M$ due to the entrance of the vortex into S_1 ($L_1 = 1$ and $L_2 = 2$) (see Figure 2b (right)); this was also made clear by comparing points (a) and (b) in Figure 2 (left). This behavior was confirmed when the next two states were compared, as the state in S_1 remained $L_1 = 1$ while $L_2 = 4$ (see Figure 2 (right) and (left) point (c)); then, $L_1 = 2$ and $L_2 = 3$ (see Figure 2 (right) and (left) point (d)).

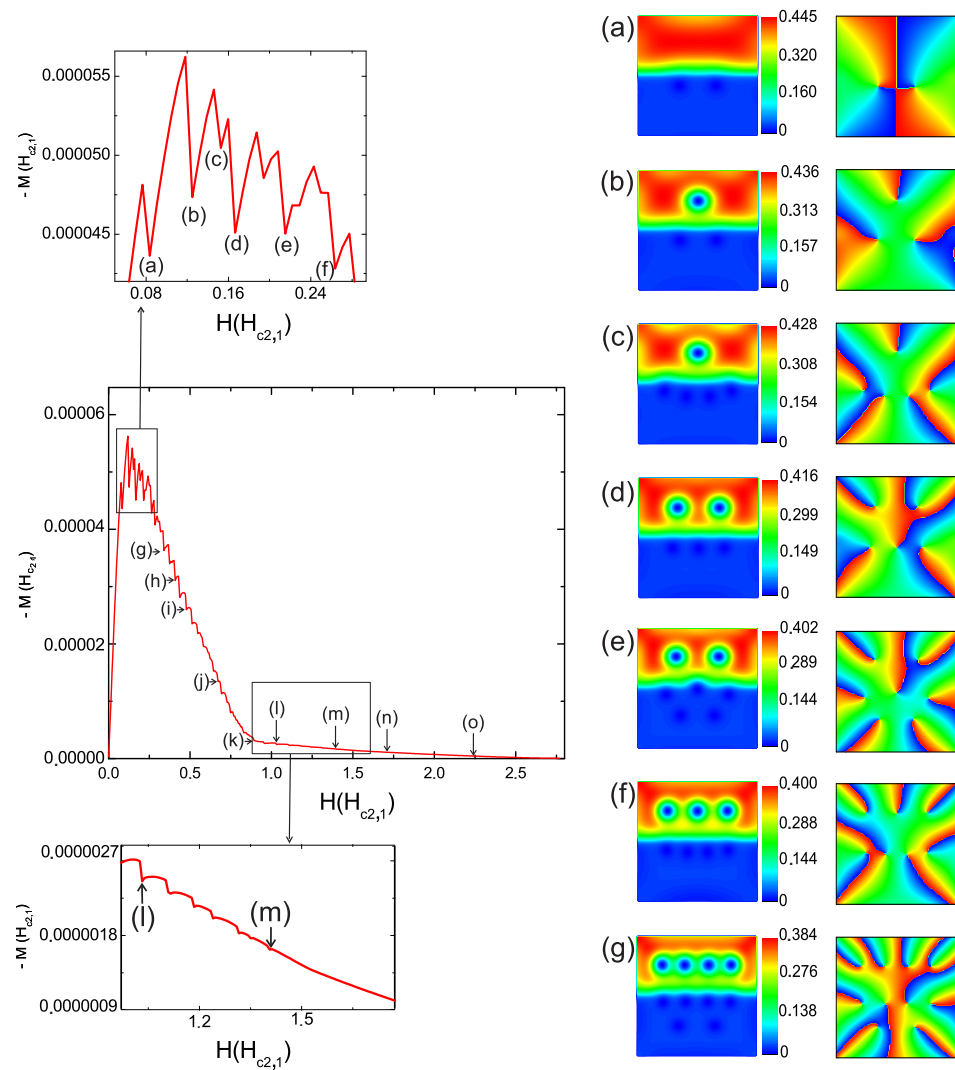


Figure 2. (Color online) **(Left)** The curve represents the magnetization as a function of an applied magnetic field H for a type II/type II superconducting square sample with $a = 400$ nm and a width of $d = 20$ nm. **(Right)** Contour plots of the density of the superconducting order parameter for different selected vortex states which correspond to the selected points on the magnetization curve named with letters from **(a–g)**; the upper section of the simulated sample is S_1 , and the characteristic lengths are $\xi_1(0) = 39$ nm and $\lambda_1(0) = 52$ nm, whereas the lower section is S_2 with $\xi_2(0) = 20$ nm, $\lambda_2(0) = 200$ nm (first column), and the corresponding phase of the order parameter (second column).

For the six points (a–f) of the magnetization curve that were selected, the entry of the magnetic flux (Φ) and the variation in the magnetization (ΔM) are given in Table 1. The range of the applied magnetic field that was considered was from $H = 0$ to $H = 0.268H_{c2,1}(0)$, where the magnetization jumps were more pronounced (see the snapshot in Figure 2 (top)). It was observed that points (b) and (d) showed larger variations in the magnetization ($-M$); only one vortex penetrated into S_1 from S_2 , and the entry of flux (Φ) could represent this behavior (see Table 1). Similar behaviors were observed in points (e) and (f), where a single vortex also penetrated into S_1 , but at the same time, two vortices penetrated S_2 , resulting in lower values of Φ than those of points (b) and (d). Although only one vortex penetrated S_1 in the transitions of (b)–(d) and (e)–(f), there were differences in the values of ΔM and Φ_0 due to the number of vortices that penetrated S_2 , which reduced the internal values of the superconducting condensate; therefore, the magnetization and magnetic flux were reduced (see Table 1).

Table 1. The vortex states in S_1 and S_2 , the applied magnetic field $H/H_{c2,1}(0)$, the entry of magnetic flux $\Phi/H_{c2,1}(0)\xi_1^2 \times 10^{-4}$ into the sample, and the variations in magnetization $\Delta M/H_{c2,1} \times 10^{-5}$ that we obtained for the magnetization curve (Figure 2). The superconducting square sample had a length of $a = 400$ nm and a width of $d = 20$ nm. For S_1 , the characteristic lengths were $\xi_1(0) = 39$ nm and $\lambda_1(0) = 52$ nm; for S_2 , they were $\xi_2(0) = 20$ nm and $\lambda_2(0) = 200$ nm.

Point	L_1	L_2	Φ	ΔM
(a)	0	2	2.32	0.455
(b)	1	2	4.67	0.893
(c)	1	4	1.91	0.364
(d)	2	3	3.76	0.715
(e)	3	4	2.574	0.522
(f)	4	6	2.571	0.489

One consequence of simulating a superconductor system with two superconducting samples is that it is necessary to obtain two upper-critical magnetic fields: $H_{2,1}(0)$ and $H_{2,2}(0)$. These values are determined in a superconductor system by using the following equation:

$$H_2(0) = \frac{H_{2,2}(0)}{\sqrt{2}\kappa_2} = \frac{\xi_1^2}{\xi_2^2} H_{2,1}(0). \tag{5}$$

For S_1 , we obtained $H_2 = 0.268H_{2,1}$, while for S_2 , we obtained $H_2 = 0.530H_{2,1}$; thus, S_1 would reach its normal state before S_2 , which implied that one half of the hybrid superconductor would behave as a metal in the normal bonded state, with the other half still being in the superconducting state. This is similar to the behavior of a superconductor sample with Newman boundary conditions. This was reflected in the behavior of the magnetization curve (Figure 2 (left)), where from point (g) to approximately point (k) was the section in which the peaks corresponded to the magnetization for one superconductor. In addition, we calculated (third critical field) $H_3(0) = 0.8962H_2(0)$, which was related to the surface superconductivity from the relation $H_3(0) = 1.69H_2(0)$. We noticed that the curve continued to decline beyond the value of H_3 from point (k) in the magnetization curve until it reached zero. This reflected that the existence of regions in the superconducting state in the sample did not display the typical surface superconductivity. From point (k), one can expect that the magnetization curve (Figure 2 (left)) would continue with the same inclination and reach the normal state at H_2 , which would be less than that reached in this case of $H_2 \approx 2.5H_2(0)$.

How do the vortex states look in a hybrid superconducting sample with square geometry? High values of the order parameter $|\Psi|^2$ are indicated by red regions, whereas lower values are indicated by blue regions. It is known that the coherence length is the scale of the characteristic length over which $|\Psi|^2$ is normalized, and it is related to the size of the vortex core. Therefore, it is intuitive that the size of the vortices will change when they penetrate from one superconductor into another, as shown in the following figures depicting vortex states.

Figure 2 (right) (a–f) shows the density of the order parameter for vortex states with different values of L_1 and L_2 in each superconductor. For $L_2 = 2$ and $L_1 = 0$, the entry of the first vortex took place in S_2 at $H = 0.083H_{c2,1}$, as shown in Figure 2 (right) (a). These vortices penetrated through the component with a lower value of $|\Psi|^2$. In the next state (Figure 2 (right) (b)), $L = 1$ in S_1 and $L = 1$ in S_2 , which meant that one new vortex penetrated S_2 , and one vortex did the same in S_1 from S_2 at $H = 0.125H_{c2,1}$.

In this state, the biggest variations in the magnetization and entry of flux were reached (Table 1 (b)). For $L_2 = 4$ and $L_1 = 1$, there were two more vortices in S_2 that joined the others close to the boundary between the two components. Once the vortices penetrated S_2 , they moved away from the screening currents in their boundary, but the vortices could not reach the middle of the sample due to the screening currents of S_1 . Additionally, despite the vortex

states of $L_2 = 4$ and $L_1 = 1$ (Figure 2 (right) (c)), only two vortices penetrated S_2 , as in the states of $L_2 = 2$ and $L_1 = 1$ (Figure 2 (right) (b)); the variations in the magnetization and flux were minor in comparison with those of the states in Figure 2 (right) (b) (see Table 1).

Figure 3g–k displays the transitions from point (g) at $H = 0.332H_{c2,1}$ to (k) at $H = 0.875H_{c2,1}$ (Figure 2 (top)). Because the size of the vortices in S_1 was larger than that of the vortices in S_2 , taking into account that the vortex radii were dependent on the coherence length ($\xi_1(0) = 39$ nm and $\xi_2(0) = 20$ nm), S_1 reached the normal state before S_2 did (see Figure 3l). Then, vortex entry from S_1 , which already achieved the normal state, into S_2 occurred; this increased the number of vortices inside it (see Figure 3m). In contrast, a superficial condensate was obtained in S_1 (see Figure 3n), and finally, this was found only in the corners of S_2 (see Figure 3o) until the total normal state was reached.

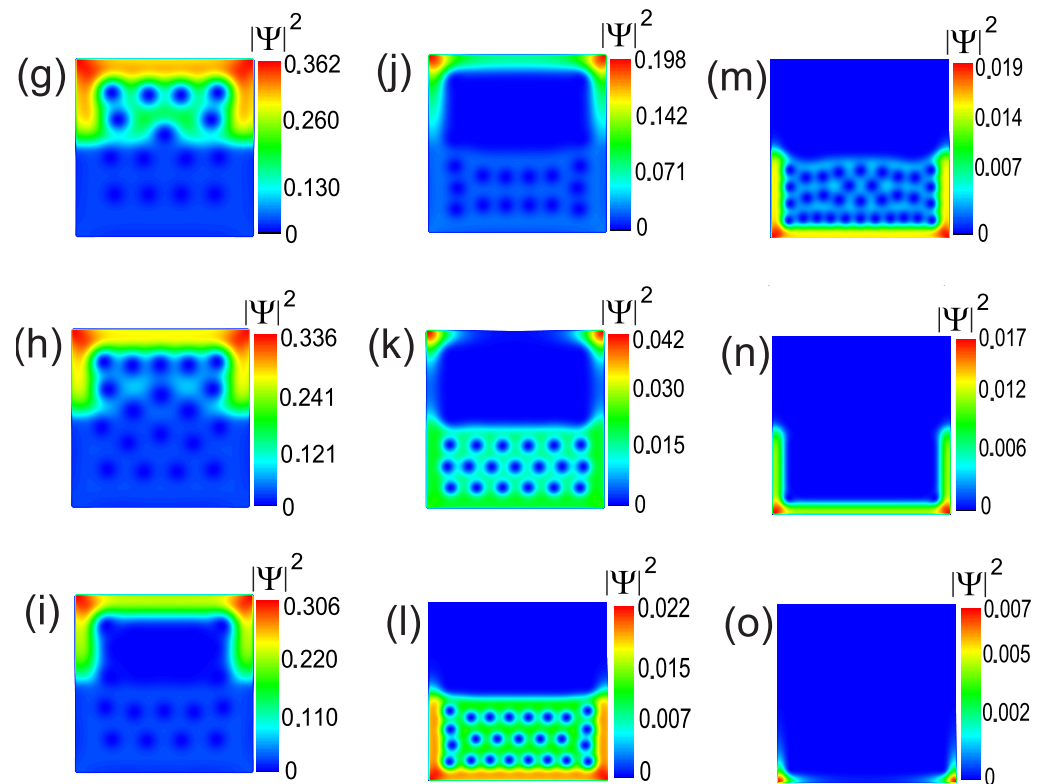


Figure 3. (g–i) (Color online) Contour plots of the superconducting order parameter for selected vortex states that show that the vortices move from S_1 to S_2 with larger values of the applied magnetic field, when considering the case analyzed in Figure 2 to follow the evolution of the behavior of the vortex state. Snapshots (l–o) show contour plots of the superconducting order parameter for selected vortex states; these show the vortices that correspond to the lower jumps in the magnetization curve. The simulation corresponds to a type II/type II superconducting square sample with $a = 400$ nm and a width of $d = 20$ nm. The characteristic lengths for S_1 are $\xi_1(0) = 39$ nm and $\lambda_1(0) = 52$ nm, and for S_2 , they are $\xi_2(0) = 20$ nm and $\lambda_2(0) = 200$ nm.

Figure 4 shows the characteristic curves of the vorticity as a function of the applied magnetic field. The numbers of vortices in each component of the hybrid superconducting sample were N_1 (S_1) and N_2 (S_2). As a result of the presence of two superconductors in the same sample, the vortex transitions followed distinct dynamics in each case, but when following the curves for each component, we found that the number of vortices in S_2 increased and decreased, while that in S_1 only increased. The number of vortices was the same in both components for several values of H (see Figure 4c (inset)) in the state where $N_2 = 8$ and $N_1 = 8$. Therefore, the values of the order parameters in both components behaved similarly for a certain range of values of H . Finally, as is more clearly shown in the inset of Figure 4d, it is interesting to note the inversion of the curves and, with

it, the variation in the number of vortices on each side of the hybrid superconductor, as evidenced in the state where $N_2 = 10$ and $N_1 = 14$ at $H = 0.512H_{c2,1}$. Here, the number of vortices was lower in S2 than in S1, and N_1 always grew. This result was because the superconducting condensate depreciated almost everywhere in S1; the screening currents decreased, causing a greater increase in the number of vortices in S1 that penetrated from S2.

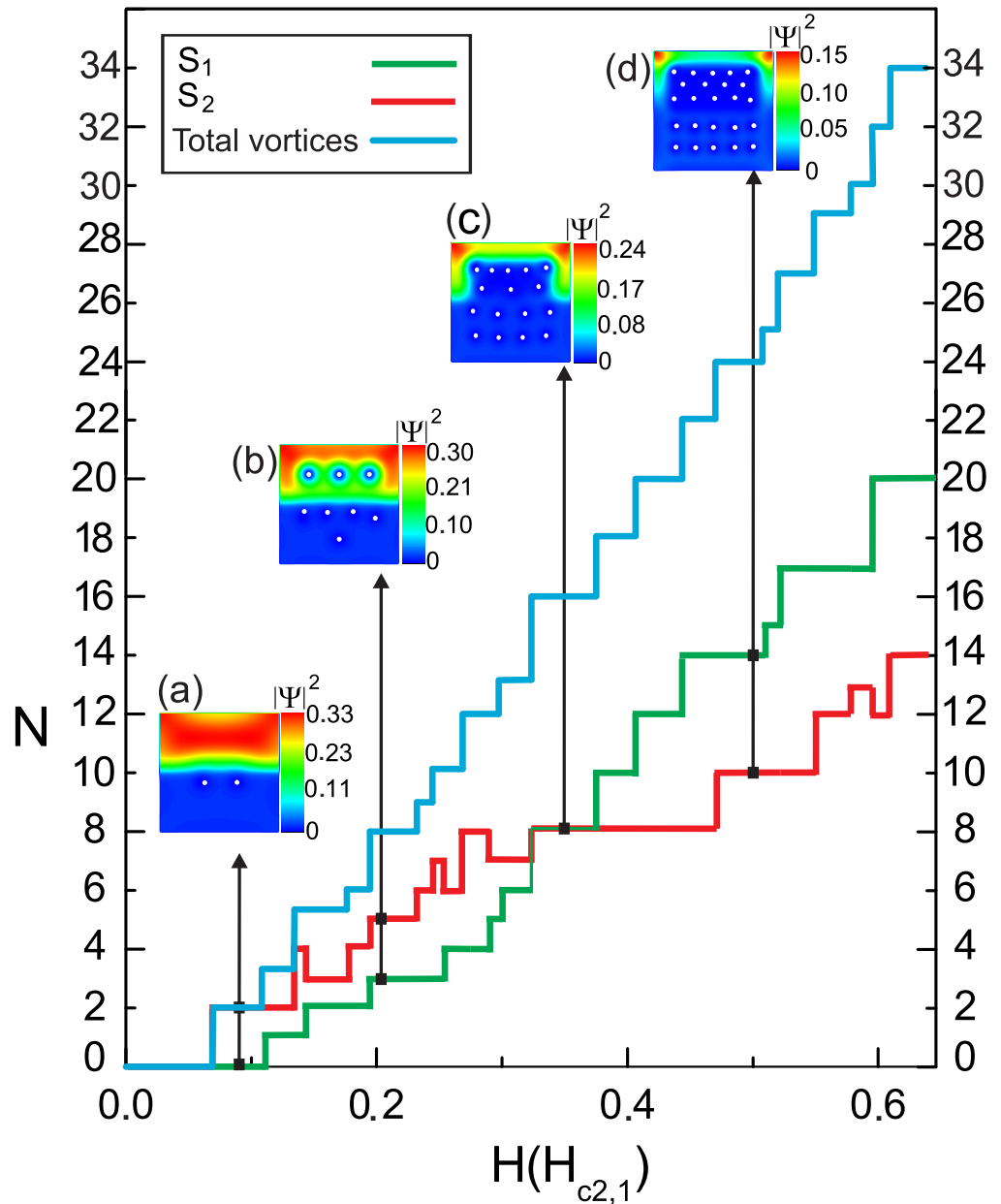


Figure 4. (Color online) The curve represents the vorticity as a function of the applied magnetic field H for a type II/type II superconducting square sample with $a = 400$ nm and a width of $d = 20$ nm. The characteristic lengths for S1 are $\xi_1(0) = 39$ nm and $\lambda_1(0) = 52$ nm, and those for S2 are $\xi_2(0) = 20$ nm and $\lambda_2(0) = 200$ nm.

Figure 5 shows the behavior of the supercurrent density, and the size of the vortices in each component can be observed.

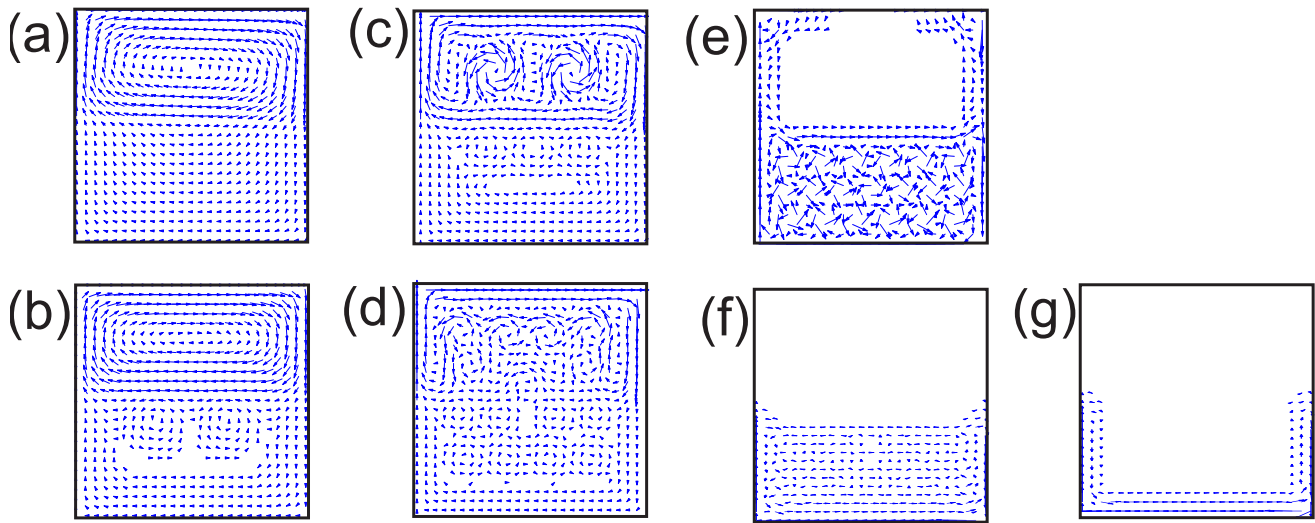


Figure 5. (a–g) (Color online) The corresponding simulation of the behavior of the supercurrent for different selected vortex states in a type II/type II superconducting square sample with $a = 400$ nm and a width of $d = 20$ nm. The characteristic lengths for S_1 were $\xi_1(0) = 39$ nm and $\lambda_1(0) = 52$ nm, and those for S_2 are $\xi_2(0) = 20$ nm and $\lambda_2(0) = 200$ nm.

Figure 5a–g shows the vector plots (blue arrows) of the supercurrent in the superconducting square with two components for the states at $H = 0.02H_{c2,1}$, $H = 0.083H_{c2,1}$, $H = 0.167H_{c2,1}$, $H = 0.263H_{c2,1}$, $H = 0.688H_{c2,1}$, $H = 1.035H_{c2,1}$, and $H = 1.713H_{c2,1}$, respectively. In Figure 5a, it is clear that the supercurrent in the sample flowed clockwise, but it changed its magnitude in S_1 and S_2 , thus proving the existence of two kinds of components in the same sample under the same applied magnetic field. Therefore, it was possible to see that the current was larger in S_1 than in S_2 , and this explained why the vortex entry occurred in S_2 first. The size of the current is indicated by the length of the arrows flowing counterclockwise around the vortex in the center. Figure 5b,c show the differences between the sizes of the currents around the vortices in S_1 and S_2 , which are directly related to the quantization flux in each component; they are also reflected in the variations in the measurement of the magnetization in the sample (see Figure 2) when the vortex penetrated into S_1 from S_2 .

Now, a hybrid system is considered in which the parameters were selected to simulate a type II superconductor and a type I superconductor; the size of the superconducting sample was $a = 400$ nm and $d = 20$ nm. The following parameters were chosen for S_1 and S_2 : a coherence length of $\xi_1(0) = 39$ nm and $\xi_2(0) = 120$ nm, a penetration depth of $\lambda_1(0) = 52$ nm and $\lambda_2(0) = 72$ nm, and a critical temperature of $T_{c1} = 9.25$ K and $T_{c2} = 8.0$ K. The temperature used in the system was $T = 6$ K, and the parameters were $c_\xi = 9.46$, $c_\lambda = 1.91$, $c_T = 1.15$, $\tau = 0.65$, and $c_m = 1$. In this analysis, we are interested in the magnetization behavior of a hybrid superconductor when one of the halves (S_2) is a type I superconductor, while S_1 retains the same parameters. In addition, in this case, the profile of the magnetization in response to the applied magnetic field variations is not typical.

In the present case, the first vortex state was obtained ($L_2 = 1$ and $L_1 = 0$) (Figure 6a) at $H = 0.036H_{c2,1}$, but as in the previous case, the magnetization did not decrease after reaching its first vortex entrance. For the two next vortex states— $L_2 = 2$ with $L_1 = 0$ at $H = 0.063H_{c2,1}$ and $L_2 = 2$ with $L_1 = 0$ at $H = 0.088H_{c2,1}$ —the curve showed an increase in the magnetization (Figure 6b,c). At the same time, the peaks shown in (a–c) displayed a decrease in magnetization until the top of the curve was reached. It is clear that the increase in magnetization was due to S_1 , while vortices that penetrated S_2 , which still increased with every step of H , as a consequence of the magnetization did not start to decay with the entry of the first vortex into S_2 . However, following peaks were reduced because of every vortex that penetrated S_2 . As a result of this, it was shown that the thin hybrid

superconductor made of type I/type II compounds displayed unconventional magnetic properties that have no counterparts in single-component systems.

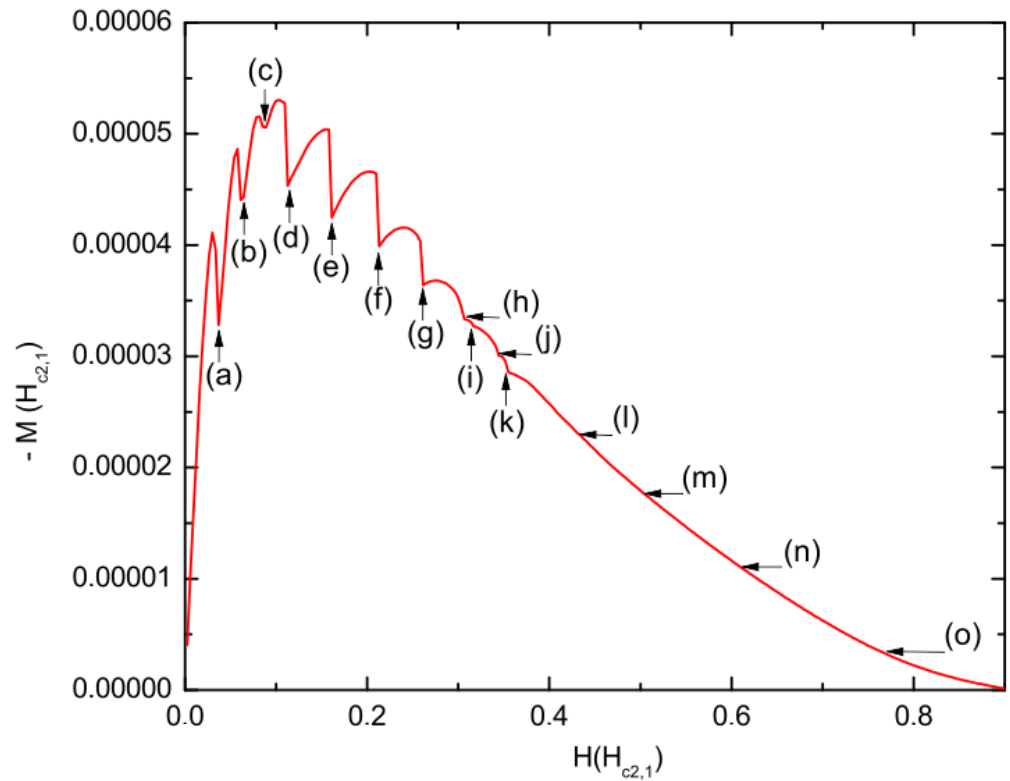


Figure 6. The curve represents the magnetization as a function of the applied magnetic field H for a type II/type I superconducting sample. The size of the superconducting sample is $a = 400$ nm and $d = 20$ nm. The following parameters are chosen for S_1 and S_2 : a coherence length of $\xi_1(0) = 39$ nm and $\xi_2(0) = 120$ nm and a penetration depth of $\lambda_1(0) = 52$ nm and $\lambda_2(0) = 72$ nm.

In points (d–g) of Figure 6, the number of vortices entering S_1 was $L_1 + 1$, and a similar situation occurred in points (b,d–f) of Figure 2. However, in the case of the type II/type II sample, there were peaks between these points; therefore, the magnetization curve shows the changes due to the entry of vortices into S_2 . Nevertheless, this did not occur in our case with the type I/type II sample; the changes were not noticeable because the magnetization dropped off faster in S_2 than in S_1 , where a normal state was reached at $H = 0.124H_{c2,1}$ and $H = 0.530H_{c2,1}$, respectively. Additionally, superficial superconductivity remained in the sample until the value of the applied magnetic field reached $H = 0.896H_{c2,1}$.

This behavior was related to the parameters that were selected to simulate S_1 and S_2 in the same sample; this can be explained with Equation (2). In this case, $1/c_\lambda = 1.91$ and $1/c_m = 1.0$, which meant that $\psi_{\infty,2}^2$ was lower than $\psi_{\infty,1}^2$. Therefore, as in the previous section for the case of the type II/type II sample, transitions with large variations in the magnetization curve were produced in S_1 , whereas small variations were produced in S_2 . For the six selected points (a–g) on the magnetization curve, the vortex states in S_1 (L_1) and S_2 (L_2), the entry of magnetic flux, and the variations in the magnetization (ΔM) are given in Table 2. It is noticeable that the values of the entry of flux (Φ_0) at points (a–c) in Figure 6 showed a reduction in the peaks of the magnetization curve, whereas at point (d), ΔM and Φ_0 grew again; then, these quantities decreased once again (see points (d–g) in Table 2). Points (a–c) in Figure 7 show the vortex configuration that was obtained for a very strong type I superconductor (S_2) in one half, whereas the other half was occupied by a type II superconductor (S_1). With low fields, we observed a configuration of vortices in only S_2 , which was indicative that the value of the supercurrent was lower than that in S_1

(see Figure 7a). A value of ξ_2 that was larger than that of λ_2 was selected for the simulation of the type I superconductor in this sample, and ξ_2 is why the size of vortices increased, thus allowing fewer vortices in S_2 in comparison with the case of the type II/type II sample. In consequence, the superconductivity quickly depreciated in S_2 , as can be seen in the first column in Figure 7c, where there were only three vortices. The number of vortices can be noticed in the second column of the phase of the order parameter in the same figure. This depreciation could also be noticed in the diminution of the supercurrent in S_2 , which was represented by arrows in this simulation; these disappeared in some regions of the sample, which implied that these regions were in the normal state (see Figure 7, third column). Moreover, in Figure 7, it is noticeable that the magnetization increased despite the entry of vortices into the sample, and the first three peaks decreased. This behavior of the magnetization curve can be explained by the snapshots of the supercurrent because as the applied magnetic field increased, it significantly decreased in S_2 , while in S_1 , it still contributed to the increase in magnetization.

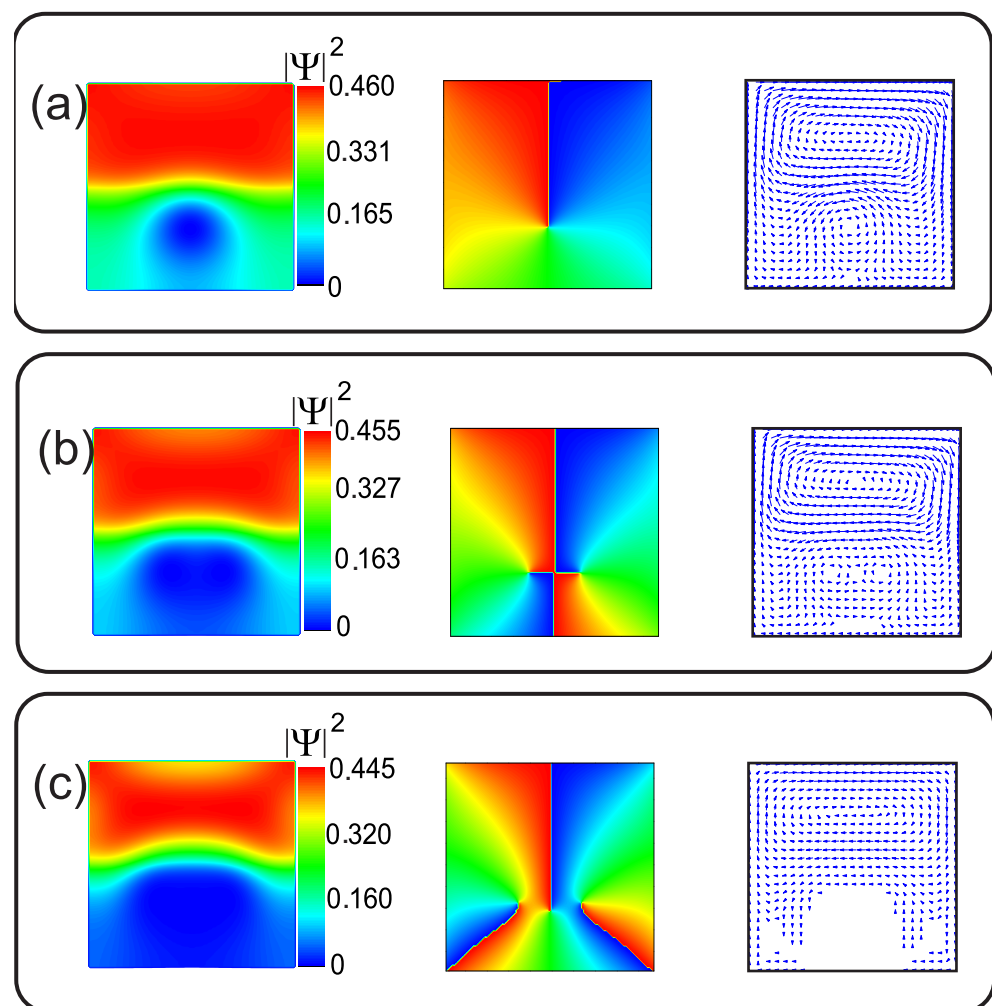


Figure 7. (a–c) (Color online) Contour plots of the density of the superconducting order parameter for different selected vortex states (first column), the phase of the order parameter (second column), and the supercurrent corresponding to the first three vortex states in the sample (third column). The size of the considered superconducting sample is $a = 400$ nm and $d = 20$ nm. The following parameters are chosen for S_1 and S_2 : a coherence length of $\xi_1(0) = 39$ nm and $\xi_2(0) = 120$ nm and a penetration depth of $\lambda_1(0) = 52$ nm and $\lambda_2(0) = 72$ nm.

Table 2. The vortex states in S_1 and S_2 , the applied magnetic field $H/H_{c2,1}(0)$, the entry of magnetic flux $\Phi_0/H_{c2,1}(0)\xi_1^2 \times 10^{-4}$ into the sample, and the variations in magnetization $\Delta M/H_{c2,1} \times 10^{-5}$ that we obtained for the magnetization curve shown in Figure 6 (points (a–g)). The size of the considered superconducting sample was $a = 400$ nm and $d = 20$ nm. The following parameters were chosen for S_1 and S_2 : a coherence length of $\xi_1(0) = 39$ nm and $\xi_2(0) = 120$ nm and a penetration depth of $\lambda_1(0) = 52$ nm and $\lambda_2(0) = 72$ nm.

Point	L_1	L_2	H	Φ	ΔM
(a)	0	1	0.038	4.328	0.824
(b)	0	2	0.063	2.363	0.450
(c)	0	3	0.088	0.493	0.094
(d)	1	3	0.110	4.242	0.807
(e)	2	5	0.161	4.164	0.792
(f)	3	7	0.211	3.430	0.653
(g)	4	9	0.260	2.689	0.512

As shown in Figure 7, it was possible to approximate the position of the vortex in each component of the phase of the order parameter at the endpoint, which is shown by a change from blue to red in the figure. If the figures of the superconducting current density are overlaid with the corresponding phase of the order parameter, they must match the center of the vortex and the endpoint of the phase (see Figure 7, second column). The relevant results of the inclusion of a type I superconductor in the sample show that the value of H at which the first entry of a vortex into S_1 occurred could be modified by choosing the correct S_2 for the other half. This possibility offers multiple options for controlling the magnetization, as well as the inputs of vortices, in a hybrid superconductor for the specific design of superconducting electronic devices.

4. Conclusions

In summary, we presented a theoretical Ginzburg–Landau (GL) study of a hybrid heterostructure made of two superconducting components. Novel and rich magnetization curves, the density of the supercurrent, and the vortex configurations in a type II/type II sample and a type I/type II sample were discussed; both kinds of samples can be engineered with proper choices of the constituent components by tuning the type II and type I properties to influence the transitions of vortex matter. The proposed superconducting system is, in many ways, peculiar and different, as the competing interactions in each component are related to the choice of the ratio for their characteristic lengths (c_λ, c_ξ), critical temperatures (c_T), and electron mass (c_m). Our superconducting system is controllable and allows for convenient vortex imaging and the detection of transitions between phases by using experimental methods. Moreover, this system opens a further research direction involving the study of three-dimensional systems with novel two-component configurations by using weak links or magnetic materials between them, thus making our system a very interesting testbed for a plethora of new phenomena.

Author Contributions: J.G. conducted the GL equations for the hybrid superconductor and performed the simulations; A.M. prepared the figures; software, J.G.; formal analysis, J.G.; writing—original draft preparation, L.C. and J.G. All authors have read and agreed to the published version of the manuscript.

Funding: This research was funded by the Universidad del Magdalena (Fonciencias) and Dirección de Investigación (Colombia).

Data Availability Statement: Data are contained within the article.

Conflicts of Interest: The authors declare no conflict of interest. The funding sponsors had no role in the design of the study, in the collection, analysis, or interpretation of data, in the writing of the manuscript, or in the decision to publish the results.

Appendix A. Theoretical Approach

In this section, we describe a numerical approach for solving the coupled Ginzburg–Landau (GL) equation. The numerical approach is based in the link variable for vector potential, which is used to discretize the two GL equations on a rectangular lattice and solve them self-consistently. The second GL equation is solved using the Fast Fourier transformation, being a Poisson-type equation.

Appendix A.1. Dimensionless Formulas in the Ginzburg–Landau Theory

Dimensionless form of the Free Energy Functional in a Hybrid System

In order to make the GL equations dimensionless, scaling quantities will be chosen. Since our sample contains two types of superconducting material, one of the components has to be chosen to base the units on. The component to be used as a base component can be arbitrary, although later, some aspects need to be taken into account with regard to making this choice. In this work, we will denote the two superconductors as S_1 and S_2 , and all the quantities will be in units depending solely on the parameters of S_1 .

$$F = \sum_{i=1,2} \int dV [\alpha_i(0) \left(1 - \frac{T}{T_{c,i}}\right) |\Psi|^2 + \frac{\beta_i}{2} |\Psi|^4 + \frac{1}{2m_i^*} \times \left| \left(-i\nabla - \frac{2e}{c} \mathbf{A}\right) \Psi \right|^2 + \frac{(\mathbf{H} - \mathbf{H}_a)^2}{8\pi}] \quad (A1)$$

With \mathbf{H} , the response of the superconductor on the applied magnetic field (\mathbf{H}_a), $\alpha(0) < 0$, where the index i represents either S_1 or S_2 depending on the location inside the volume V . The GL equations will be scaled to the parameters of S_1 , with the variables α_1 , β_1 , and m_1^* . Distance will be measured in units of $\xi_1(0) = \sqrt{-\hbar^2/2m_1^*\alpha_1(0)}$, the temperature in units of the critical temperature of S_1 ($T_{c,1}$), the order parameter Ψ in units of $\Psi_{\infty,1} = \sqrt{-\alpha_1(0)/\beta_1}$, the vector potential in units of $A_{0,1} = c\hbar/2e\xi_1(0)$, the magnetic field in units of the upper critical field of S_1 , $H_{c2,1} = c\hbar/2e\xi_1^2(0)$, and the free energy in units of $F_0 = \alpha_1^2(0)/\beta_1$. This is conducted by transforming the variables as follows:

$$\begin{aligned} \mathbf{r} &\longrightarrow \xi_1(0) \mathbf{r}', \\ \nabla &\longrightarrow \frac{1}{\xi_1(0)} \nabla', \\ \Psi(\mathbf{r}) &\longrightarrow \Psi_{\infty,1} \psi(\mathbf{r}'), \\ \mathbf{A} &\longrightarrow A_{0,1} \mathbf{A}', \\ \mathbf{H} &\longrightarrow H_{c2,1} \mathbf{H}', \\ V &\longrightarrow \xi_1^3(0) V', \\ F &\longrightarrow F_0 \xi_1^3(0) F', \end{aligned}$$

Working on (A1), we obtain the expression for free energy in the following form:

$$F = \int dV \left[- \left(1 - \frac{T}{T_{c,i}}\right) \frac{\alpha_i(0)}{\alpha_1(0)} |\Psi|^2 + \frac{1}{2} \frac{\beta_i}{\beta_1} |\Psi|^4 - \frac{\hbar^2}{2m_1^* \xi_1^2(0) \alpha_1(0)} |(-i\nabla - \mathbf{A}) \Psi|^2 + \frac{H_{c2,1}^2}{F_0} \frac{(\mathbf{H} - \mathbf{H}_a)^2}{8\pi} \right]. \quad (A2)$$

By using the fact that $\xi_i(0) = \sqrt{-\hbar^2/2m_i^*\alpha_i(0)}$ and that $\kappa_1^2 = H_{c2,1}^2/8\pi F_0 = m^2 c^2 \beta - 1/8\pi \hbar^2 e^2$, we obtain the following form for the free energy of our system:

$$F = \int dV \left[- \left(1 - \frac{T_{c,1}}{T_{c,i}} \frac{T}{T_{c,i}}\right) \frac{m_1^* \xi_1^2(0)}{m_i^* \xi_i^2(0)} |\Psi|^2 - \frac{1}{2} \left(\frac{m_1^*}{m_i^*}\right)^2 \frac{\lambda_i^2(0) \xi_1^2(0)}{\lambda_1^2(0) \xi_i^2(0)} + \frac{m_1^*}{m_i^*} |(-i\nabla - \mathbf{A}) \Psi|^2 + \kappa_1^2 (\mathbf{H} - \mathbf{H}_a)^2 \right]. \quad (A3)$$

Next, variable $t = T/T_1^*$ and ratios $c_T = T_{c,1}/T_{c,2}$, $c_\lambda = \lambda_2^2(0)/\lambda_1^2(0)$, $c_\xi = \xi_2^2(0)/\xi_1^2(0)$, and $c_m = m_1^*/m_2^*$ are defined. Equation (A3) now takes the form:

$$F = \int dV [-(1 - c_T t \frac{c_m}{c_\xi}) |\Psi|^2 + \frac{1}{2} \frac{c_\lambda c_m^2}{c x i} |\Psi|^4 + c_m |(-i\nabla - \mathbf{A})\Psi|^2 + \kappa_1^2 (\mathbf{H} - \mathbf{H}_a)^2], \quad (\text{A4})$$

where c_m , c_ξ , c_λ , and c_T are equal to 1 inside S_1 material.

Appendix A.2. Derivation of GL Equations in a Hybrid System

Appendix A.2.1. First GL Equation

An infinitesimal change of order parameter $\delta\psi$ with which the free energy should remain invariant ($\delta F = 0$), i.e.,

$$\delta F = \int_{V_s} dV [-(1 - c_T t) \frac{c_m}{c_\xi} \psi \delta\psi^* + \frac{c_\lambda c_m^2}{c_\xi} |\Psi|^2 \psi \delta\psi^* + c_m (\mathbf{\Pi}\psi) \cdot (\mathbf{\Pi}^* \delta\psi^*)] + c.c. = 0. \quad (\text{A5})$$

We introduced the canonical momentum operator $\mathbf{\Pi} = -i\nabla - \mathbf{A}$. The last term of Equation (A5) can be simplify by using the relationship $\nabla \cdot (c\mathbf{v}) = \mathbf{v} \cdot \nabla c + c\nabla \cdot \mathbf{v}$, where c is a scalar, but also, taking into account Gauss's theorem ($\int \nabla \cdot \mathbf{N} = \oint dS \mathbf{n} \cdot \mathbf{N}$, with \mathbf{n} as the unit vector perpendicular to the surface), we obtain:

$$\delta F = \int_{V_s} dV \delta\psi^* [-(1 - c_T t) \frac{c_m}{c_\xi} \psi + \frac{c_\lambda c_m^2}{c_\xi} |\Psi|^2 \psi + c_m \mathbf{\Pi}^2 \psi] = i \oint dS [\mathbf{n} \cdot \mathbf{\Pi}\psi] + c.c. = 0. \quad (\text{A6})$$

The fact that this equation must hold for arbitrary $\delta\psi^*$ means that the terms between brackets have to be 0. This leads to the first GL equation:

$$-(1 - c_T t) \frac{1}{c_\xi} \psi + \frac{c_\lambda}{c_\xi} |\psi|^2 \psi + \mathbf{\Pi}^2 \psi = 0, \quad (\text{A7})$$

where $c_m = 1$ and the boundary condition:

$$\mathbf{n} \cdot \mathbf{\Pi}\psi|_{S_s}. \quad (\text{A8})$$

Appendix A.2.2. Second GL Equation

In order to derive the second GL equation, the vector potential will be varied by $\delta\mathbf{A}$. The part of free energy containing the magnetic field then gives:

$$F_M(\mathbf{A} + \delta\mathbf{A}) = \int dV [c_m |(\mathbf{\Pi} - \delta\mathbf{A})\psi|^2 + \kappa_1^2 (\nabla \times (\mathbf{A} + \delta\mathbf{A} - \mathbf{A}_0))^2]. \quad (\text{A9})$$

We considered $\mathbf{H} = \nabla \times \mathbf{A}$ and $\mathbf{H}_a = \nabla \times \mathbf{A}_0$, where \mathbf{H}_a is the applied magnetic field. Now, since $F_M(\mathbf{A} + \delta\mathbf{A}) \approx F(\mathbf{A}) + \delta F$, we can separate the terms that are linear in $\delta\mathbf{A}$ to find δF :

$$\begin{aligned} \delta F &= \int dV [c_m (-\delta\mathbf{A}(\psi^* \mathbf{\Pi}\psi)) - \delta\mathbf{A}(\psi \mathbf{\Pi}^*)\psi^*) + 2\kappa_1^2 (\nabla \times (\mathbf{A} - \mathbf{A}_0))(\nabla \times \delta\mathbf{A})] \\ &= \int dV [-2c_m \delta\mathbf{A} \mathbb{R}(\psi^* \mathbf{\Pi}\psi) + 2\kappa_1^2 (\nabla \times (\mathbf{A} - \mathbf{A}_0)) \cdot (\nabla \times \delta\mathbf{A})]. \quad (\text{A10}) \end{aligned}$$

The second part of Equation (A10) can be rewritten by using the Stock's theorem ($\nabla(\mathbf{a} \times \mathbf{b}) = \mathbf{b} \cdot (\nabla \times \mathbf{a}) - \mathbf{a} \cdot (\nabla \times \mathbf{b})$) as

$$\delta F = \int dV [2\kappa_1^2 (\nabla(\delta\mathbf{A} \times (\nabla \times (\mathbf{A} - \mathbf{A}_0))) + \delta\mathbf{A} \cdot (\nabla \times \nabla \times (\mathbf{A} - \mathbf{A}_0))]. \quad (\text{A11})$$

The first part of Equation (A12) can be modified into a surface integral using Gauss's theorem. Since the surface lies at infinity, $\mathbf{A} = \mathbf{A}_0$; thus, the contribution of the surface integral vanishes. The variation of the free energy becomes:

$$\delta F = 2 \int dV \delta \mathbf{A} \left[-c_m \mathbb{R}(\psi^* \mathbf{\Pi} \psi) + \kappa_1^2 (\nabla \times \nabla \times (\mathbf{A} - \mathbf{A}_0)) \right] = 0. \quad (\text{A12})$$

This equation should hold for arbitrary $\delta \mathbf{A}$. This can only be the case if the term between square brackets is zero. This yields the second Ginzburg–Landau equation:

$$\mathbf{j}_s = c_m \mathbb{R}(\psi^* \mathbf{\Pi} \psi) = \kappa_1^2 (\nabla \times \nabla \times (\mathbf{A} - \mathbf{A}_0)), \quad (\text{A13})$$

where \mathbf{j}_s is the supercurrent, induced in the superconductor, in response to the applied magnetic field. The equation can be further reduced after choosing the Coulomb gauge $\nabla \cdot (\mathbf{A} - \mathbf{A}_0) = 0$.

References

- de Gennes, P.G. Boundary effects in superconductors. *Rev. Mod. Phys.* **1964**, *36*, 225. [[CrossRef](#)]
- Buzdin, A.I. Proximity effects in superconductor-ferromagnet heterostructures. *Rev. Mod. Phys.* **2005**, *11*, 935–976. [[CrossRef](#)]
- Baelus, B.J.; Partoens, B.; Peeters, F.M. One-dimensional modulation of the superconducting boundary condition for thin superconducting films. *Phys. Rev. B* **2006**, *73*, 212503. [[CrossRef](#)]
- Ozaeta, A.; Vasenko, A.S.; Hekking, F.W.J.; Bergeret, F.S. Andreev current enhancement and subgap conductance of superconducting SFN hybrid structures in the presence of a small spin-splitting magnetic field. *Phys. Rev. B* **2012**, *86*, 060509. [[CrossRef](#)]
- Bergeret, F.S.; Tokatly, I.V. Singlet-Triplet Conversion and the Long-Range Proximity Effect in Superconductor-Ferromagnet Structures with Generic Spin Dependent Fields. *Phys. Rev. Lett.* **2013**, *110*, 117003. [[CrossRef](#)]
- Black-Schaffer, A.M. Self-consistent superconducting proximity effect at the quantum spin Hall edge. *Phys. Rev. B* **2011**, *83*, 060504. [[CrossRef](#)]
- Yano, R.; Hirose, H.T.; Tsumura, K.; Yamamoto, S.; Koyanagi, M.; Kanou, M.; Kashiwaya, H.; Sasagawa, T.; Kashiwaya, S. Proximity-Induced Superconducting States of Magnetically Doped 3D Topological Insulators with High Bulk Insulation. *Condens. Matter* **2019**, *4*, 9. [[CrossRef](#)]
- Karabassov, T.; Amirov, E.S.; Bobkova, I.V.; Golubov, A.A.; Kazakova, E.A.; Vasenko, A.S. Superconducting Diode Effect in Topological Hybrid Structures. *Condens. Matter* **2023**, *8*, 36. [[CrossRef](#)]
- Xu, M.; Liang, T.; Shi, M.; Chen, H. Graphene-Like Two-Dimensional Materials. *Chem. Rev.* **2013**, *113*, 3766–3798. [[CrossRef](#)]
- Perez de Lara, D. Hybrid Superconducting/Magnetic Multifunctional Devices in Two-Dimensional Systems. *Physchem* **2022**, *2*, 347–356. [[CrossRef](#)]
- Natterer, F.D.; Ha, J.; Baek, H.; Zhang, D.; Cullen, W.G.; Zhitenev, N.B.; Kuk, Y.; Stroschio, J.A. Scanning tunneling spectroscopy of proximity superconductivity in epitaxial multilayer graphene. *Phys. Rev. B* **2016**, *93*, 045406. [[CrossRef](#)] [[PubMed](#)]
- Berdiyrov, G.R.; Misko, V.R.; Milošević, M.V.; Escoffier, W.; Grigorieva, I.V.; Peeters, F.M. Pillars as antipinning centers in superconducting films. *Phys. Rev. B* **2008**, *77*, 024526. [[CrossRef](#)]
- Sharma, M.; Singh, M.; Rakshit, R.K.; Singh, S.P.; Fretto, M.; De Leo, N.; Perali, A.; Pinto, N. Complex Phase-Fluctuation Effects Correlated with Granularity in Superconducting NbN Nanofilms. *Nanomaterials* **2022**, *12*, 4109. [[CrossRef](#)] [[PubMed](#)]
- McNaughton, B.; Pinto, N.; Perali, A.; Milošević, M.V. Complex Causes and Consequences of Ordering and Dynamic Phases of Confined Vortex Rows in Superconducting Nanostripes. *Nanomaterials* **2022**, *12*, 4043. [[CrossRef](#)] [[PubMed](#)]
- Barba-Ortega, J.; González, J.D.; Sardella, E. Superconducting State of a Disk with a Pentagonal/Hexagonal Trench/Barrier. *J. Low Temp. Phys.* **2013**, *174*, 96. [[CrossRef](#)]
- Baelus, B.J.; Peeters, F.M. Mesoscopic Superconductors Multiply Connected Mesoscopic Superconductors. *Mod. Phys. Lett. B* **2003**, *17*, 527. [[CrossRef](#)]
- Baelus, B.J.; Peeters, F.M. Dependence of the vortex configuration on the geometry of mesoscopic flat samples. *Phys. Rev. B* **2002**, *65*, 104515. [[CrossRef](#)]
- Chao-Yu, L.; Berdiyrov, G.R.; Milošević, M.V. Vortex states in layered mesoscopic superconductors. *Phys. Rev. B* **2011**, *83*, 104524.
- Berdiyrov, G.R.; de C. Romaguera, A.R.; Milošević, M.V.; Doria, M.M.; Covaci, L.; Peeters, F.M. Dynamic and static phases of vortices under an applied drive in a superconducting stripe with an array of weak links. *Eur. Phys. J. B* **2012**, *85*, 130. [[CrossRef](#)]
- González, J.D.; Barón-Jaimez, J.; Barba-Ortega, J. Complex vortex configuration in a disk with a higher/lower critical temperature superconducting geometrical central defect. *J. Low Temp. Phys.* **2015**, *179*, 264. [[CrossRef](#)]
- Bouquet, F.; Fisher, R.A.; Phillips, N.E.; Hinks, D.G.; Jorgensen, J.D. Specific heat of Mg11B2: Evidence for a second energy gap. *Phys. Rev. Lett.* **2001**, *87*, 047001. [[CrossRef](#)] [[PubMed](#)]
- Geurts, R.; Milošević, M.V.; Peeters, F.M. Vortex matter in mesoscopic two-gap superconducting disks: Influence of Josephson and magnetic coupling. *Phys. Rev. B* **2010**, *81*, 214514. [[CrossRef](#)]

23. Milošević, M.V.; Perali, A. Emergent phenomena in multicomponent superconductivity: An introduction to the focus issue. *Supercond. Sci. Technol.* **2015**, *28*, 060201. [[CrossRef](#)]
24. Pinto, N.; Javad, S.; Perali, A.; Flammia, L.; Milošević, M.V.; Fretto, M.; Cassiogo, C.; De Leo, N. Dimensional crossover and incipient quantum size effects in superconducting niobium nanofilms. *Sci. Rep.* **2018**, *8*, 4710. [[CrossRef](#)]
25. Shalnikov, A. Superconducting Thin Films. *Nature* **1938**, *142*, 74. [[CrossRef](#)]
26. Strongin, M.; Kammerer, O.F. Superconductive Phenomena in Ultrathin Films. *J. Appl. Phys.* **1968**, *39*, 2509. [[CrossRef](#)]
27. Jaeger, H.M.; Haviland, D.B.; Orr, B.G.; Goldman, A.M. Onset of superconductivity in ultrathin granular metal films. *Phys. Rev. B* **1989**, *40*, 182. [[CrossRef](#)]
28. Qin, Y.; Vicente, C.L.; Yoon, J. Magnetically induced metallic phase in superconducting tantalum films. *Phys. Rev. B* **2006**, *73*, 100505. [[CrossRef](#)]
29. Qin, S.; Kim, J.; Niu, Q.; Shih, C.K. Superconductivity at the Two-Dimensional Limit. *Science* **2009**, *234*, 1314. [[CrossRef](#)]
30. Saito, Y.; Nojima, T.; Iwasa, Y. Highly crystalline 2D superconductors. *Nat. Rev. Mater.* **2017**, *2*, 16094. [[CrossRef](#)]
31. Costanzo, D.; Jo, S.; Berger, H.; Morpurgo, A.F. Gate-induced superconductivity in atomically thin MoS_2 crystals. *Nat. Nanotechnol.* **2016**, *11*, 339. [[CrossRef](#)] [[PubMed](#)]
32. Buzdin, A. Mixing superconductivity and magnetism. *Nat. Mater.* **2004**, *3*, 751. [[CrossRef](#)] [[PubMed](#)]
33. Biscaras, J.; Bergeal, N.; Hurand, S.; Feuillet-Palma, C.; Rastogi, A.; Budhani, R.C.; Grilli, M.; Caprara, S.; Lesueur, J. Multiple quantum criticality in a two-dimensional superconductor. *Nat. Mater.* **2013**, *12*, 542. [[CrossRef](#)] [[PubMed](#)]

Disclaimer/Publisher's Note: The statements, opinions and data contained in all publications are solely those of the individual author(s) and contributor(s) and not of MDPI and/or the editor(s). MDPI and/or the editor(s) disclaim responsibility for any injury to people or property resulting from any ideas, methods, instructions or products referred to in the content.